Available online at www.sciencedirect.com
SCIENCE DIRECT
International Journal of Heat and Mass Transfer 49 (2006) 777–788
International Journal of HEAT and MASS TRANSFER
www.elsevier.com/locate/ijhmt

Effects of primary soot particle size distribution on the temperature of soot particles heated by a nanosecond pulsed laser in an atmospheric laminar diffusion flame

Fengshan Liu [a,*], Barry J. Stagg [b], David R. Snelling [a], Gregory J. Smallwood [a]

[a] Combustion Technology Group, Institute for Chemical Process and Environmental Technology, National Research Council, Building M-9, 1200 Montreal Road, Ottawa, Ont., Canada K1A 0R6
[b] Columbian Chemicals Company, 1800 West Oak Commons Ct., Marietta, GA 30062, United States

Received 27 January 2005; received in revised form 13 July 2005
Available online 3 October 2005

Abstract

Temperature histories of nanosecond pulsed laser heated soot particles of different primary particle size distributions were calculated using a single primary particle based heat and mass transfer model under conditions of a typical atmospheric laminar diffusion flame. The critical peak soot particle temperatures beyond which soot particle sublimation cannot be neglected were identified to be about 3300–3400 K. Knowledge of this critical soot particle temperature is required to conduct low-fluence laser-induced incandescence experiments in which soot sublimation is avoided. After the laser pulse, the temperature of smaller primary soot particles decreases faster than that of larger ones as a result of larger surface area-to-volume ratio. Unlike the common belief that the peak soot particle temperature is independent of the primary particle diameter, the numerical results indicate that this assumption is valid only when soot sublimation is negligible and for primary soot particle diameters greater than about 20 nm. The effective temperature of a soot particle ensemble having different primary particle diameters in the laser probe volume was calculated based on the ratio of the total thermal radiation intensities of soot particles at 400 and 780 nm to simulate the experimentally measured soot particle temperature using two-color optical pyrometry. In the non-sublimation regime, the initial effective temperature decay rate after the peak soot temperature is related to the Sauter mean diameter of the primary soot particle diameter distribution. At longer times, the effective temperatures of soot particle ensembles start to display different decay rates for different soot primary particle diameter distributions. A simple approach was proposed in this study to infer the two parameters of lognormal distributed primary soot particle diameter. Application of this approach was demonstrated in an atmospheric laminar ethylene diffusion flame with the inferred primary soot particle diameter distribution compared with independent ex situ measurement.

Keywords: Laser-induced incandescence; Pulsed laser heating; Primary soot particle distribution; Nanoparticle sizing; Heat conduction in free-molecular regime

1. Introduction

Optical diagnostic techniques play an important role in our understanding of soot formation, growth, aggregation, and oxidation in flames and in characterizing the morphology of nanoparticles such as soot, diesel particulate matter, and carbon black. Compared to the more conventional techniques for soot characterization including soot volume fraction by laser extinction [1] and soot morphology (primary particle diameter and aggregate size distribution) by laser scattering [2] and thermophoretic sampling/transmission electron microscopy analysis (TS/TEM) [3], the more recently developed laser-induced incandescence (LII) techniques [4–8] offer the advantages of spatially and temporally resolved measurement. LII has been proven to be a

* Corresponding author. Tel.: +1 613 993 9470; fax: +1 613 957 7869.
E-mail address: fengshan.liu@nrc-cnrc.gc.ca (F. Liu).

0017-9310/$ - see front matter
doi:10.1016/j.ijheatmasstransfer.2005.07.041

Nomenclature

c	speed of light in vacuum, 2.9979×10^8 m/s
c_s	specific heat of soot, J/kg K
C_a	absorption cross section of soot particle, nm^2
d_{10}	arithmetic mean particle diameter, nm
d_{32}	Sauter mean particle diameter, nm
d_g	geometric mean diameter of lognormal distribution, nm
d_p	diameter of primary soot particle, nm
$E(m)$	refractive index function for absorption, $=\mathrm{Im}((m^2-1)/(m^2+2))$
F_0	laser fluence, mJ/mm^2
h	Planck constant, 6.6262×10^{-34} J s
ΔH_v	heat of vaporization of soot, J/mole
k	imaginary part of the refractive index
k_B	Boltzmann constant, 1.3806×10^{-23} J/K
m	refractive index of soot, $=n+\mathrm{i}k$
m_g	mass of the surrounding gas molecule, g
M	mass of primary soot particle, g
M_v	molecular weight of soot vapor, g/mol
n	real part of the refractive index
N_A	Avogadro's number, 6.022×10^{23} molecules/mol
N_v	molecular flux of evaporated carbon, molecules/m^2 s
p_g	ambient gas pressure, Pa
q	laser intensity, W/mm^2
q_c	rate of conduction heat loss from soot particle to the surrounding gas, W
q_{rad}	heat loss term due to radiation, W
R	universal gas constant, 8.313 J/mole K
t	time, ns
T	temperature of a single soot particle, K
T_e	effective temperature of soot particle ensemble, K
T_g	gas temperature, K

Greek symbols

α	thermal accommodation coefficient of soot
λ	wavelength, nm
$\gamma(T_g)$	specific heat ratio of air
γ^*	average specific heat ratio of air, Eq. (3)
ρ_s	density of soot, kg/m^3
σ_g	geometric standard deviation of lognormal distribution

powerful yet relatively simple diagnostic tool for measurement of soot volume fraction in a wide range of applications, such as laminar and turbulent flames, in-cylinder measurement, and engine exhaust measurement.

Beside the soot volume fraction, it is also feasible to infer the mean primary soot particle size and/or the primary soot particle size distribution from the time-resolved LII signals. The idea of particle sizing from laser-induced incandescence signals was perhaps first outlined by Weeks and Duley in 1974 [9]. They used a microsecond pulsed TEA (transverse excited atmospheric) CO_2 laser (at 10.6 μm) to excite submicron powders of carbon black and alumina. They showed both theoretically and experimentally that the peak particle temperature (also the peak incandescence signal) occurs at a time that is larger with increasing particle size. A decade later, the potential and some strategies of using LII as a soot sizing diagnostic were discussed by Melton [10]. Little or perhaps no work on the application of LII to infer soot particle size distribution was conducted between the mid-80s and the mid-90s. The first quantitative application of LII as a diagnostic for soot particle sizing was made by Will et al. [11]. Their numerically calculated time-resolved LII signal using the heat and mass transfer model of LII formulated by Melton [10] and Tait and Greenhalgh [12] indicate that signal of small particles decays faster than that of larger particles, which is fundamentally attributed to the fact that smaller particles have a larger surface area-to-volume ratio than larger ones. They showed that the ratio of the LII signals at two different times after the laser pulse can be unambiguously related to the soot primary particle diameter and was found to be weakly dependent on the laser intensity. They demonstrated the method in the measurement of soot particle diameter in a laminar ethane–air diffusion flame and obtained reasonable results. Since the work of Will et al. [11], rapid progress has been made in the last decade to explore various ways to use the time-resolved LII technique as an ultrafine particle sizing tool to infer the information of primary particle size (mean diameter and/or the distribution) [8,13–24]. In all these studies the numerical LII model plays an essential role in inferring the mean primary particle size and the primary soot particle size distribution from the experimental time-resolved LII intensities and/or time-resolved soot particle temperature measured by two-color optical pyrometry. Therefore, the accuracy of the numerical LII model, in particular the heat conduction sub-model, has significant and direct impact on the accuracy of primary particle size determined from LII measurements.

Theoretical models describing the nanoscale heat and mass transfer processes of LII have been developed and improved over the last two decades [25,26, and references cited therein]. However, significant uncertainty may still exist in the numerical results under conditions of significant soot sublimation primarily due to the lack of reliable physical parameters in the soot sublimation sub-model such as the vapor pressure and the heat of vaporization [27]. To avoid the uncertainty in the sublimation sub-model in numerical study and to make the LII technique truly non-intrusive, our recent experimental and numerical studies

[28,29] have focused on low-fluence LII, in which the maximum soot particle temperature remains below about 3500 K, ensuring negligible soot sublimation. Besides the uncertainty in the sublimation sub-model, which can be avoided by using a low-fluence laser beam, the accuracy of the mean primary soot particle diameter estimated using the experimental temperature decay rate [8] is severely limited by our knowledge of the soot particle thermal accommodation coefficient α. The values for α of soot particles cited in the literature is subjected to significant uncertainty, from 0.26 [7] to 0.9 [30]. Our recent study has determined new values of soot absorption function $E(m)$ at 1064 nm and the soot particle thermal accommodation coefficient α based on experimental temperature decay rate and known soot morphology in a laminar diffusion flame [28]. Besides the uncertainty in the physical properties of soot at high temperature, little attention has been paid in LII modeling to the potentially important impact of the so-called *shielding effect* on the calculation of the heat conduction rate between the soot aggregates and the surrounding gas [28]. Soot particles appear as mass-fractals as a result of aggregation. Although such structures are fairly open (fractal dimension about 1.8), some primary particles are still partially or even fully hidden from the exterior of the aggregate. Consequently, the available surface area for collision with the surrounding gas molecules is somewhat reduced. Due to the shielding effect, soot particles in larger aggregates have a slower overall cooling rate than those in smaller aggregates. Except for our recent studies [28,31], in which an attempt was made to formulate a more realistic aggregate-based LII model (but for monodispersed primary soot particles), to our best knowledge all the theoretical models of LII appearing in the literature were formulated for a single primary particle. However, since the primary concern of the present study is the effect of the primary soot particle diameter distribution on the temperature history of soot particle ensembles heated by a nanosecond laser pulse, the shielding effect of reduced heat transfer rate on aggregated soot particles is not taken into account. As such, the single primary soot particle based LII model is employed to conduct the numerical study. Work is in progress to develop a more sophisticated LII model for aggregated soot particles with polydispersed primary particle diameter.

The primitive variables predicted by a LII model are the time-dependent temperature and diameter of a single primary particle of prescribed initial diameter and temperature. In addition, the temporal decay rate of the soot particle temperature bears the information on its diameter. Therefore, it is highly desirable to determine the soot particle temperature experimentally for the purposes of LII model validation and/or inferring the primary particle size. A practical method to measure the temperature of particles (soot, coal, and carbon) is optical pyrometry, based on the particle thermal emission intensities detected at two or more wavelengths. When the temperature of soot particles in the measurement volume is non-uniform, the measured temperature is an *effective temperature*, which is a weighted average temperature biased toward the hottest particles. Various optical pyrometers have also been used to monitor the soot particle temperature during LII. Eckbreth [32] measured the laser-irradiated soot particle surface temperatures using the LII signals detected at two different wavelengths. Snelling et al. [8] employed a three-wavelength pyrometer to measure the laser-heated soot particle surface temperatures in a diesel engine exhaust. More recently, time-resolved two-color LII (detection of LII signals at two different wavelengths to determine the soot particle effective temperature) has received increased attention [23,28,29,33–35].

In this study numerical calculations were conducted to obtain the temperature history of soot particles of different diameters. Assuming the primary soot particle diameter distribution is log-normal, the effective temperature of soot particle ensembles in the laser probe volume was calculated based on the ratio of thermal emission intensities of soot particles at 400 and 780 nm to simulate the experimentally measured soot particle temperature using two-color optical pyrometry. The objectives of the present study are (i) to identify the critical soot particle temperature below which soot sublimation is negligible based on the best currently available thermal properties in the soot sublimation sub-model, (ii) to investigate the effect of the primary soot particle diameter distribution on the temporal decay rate of the effective soot temperature, and (iii) to propose a simple approach to infer the primary soot particle diameter distribution from the time-resolved soot particle temperature and demonstrate the approach in an atmospheric pressure laminar ethylene diffusion flame.

2. Theory

2.1. Single-particle LII model

The numerical LII model employed in the present study is largely based on our previous studies [25,27]. The energy balance equation for a single primary particle can be written as [25]

$$\frac{1}{6}\pi d_{\mathrm{p}}^3 \rho_{\mathrm{s}} c_{\mathrm{s}} \frac{\mathrm{d}T}{\mathrm{d}t} = C_{\mathrm{a}} F_0 q(t) - \dot{q}_{\mathrm{rad}} - \dot{q}_{\mathrm{c}} + \frac{\Delta H_{\mathrm{v}}}{M_{\mathrm{v}}} \frac{\mathrm{d}M}{\mathrm{d}t} \tag{1}$$

The terms in Eq. (1) represent, in order, the rate of soot particle internal energy change, the rate of laser energy absorption by the particle, the rate of heat loss due to thermal radiation, the rate of conduction heat loss from the particle to the surrounding gas, and finally the rate of heat loss due to soot sublimation. It should be mentioned that there also exist other physical and chemical processes during LII, such as photodesorption, annealing, soot oxidation etc., as discussed in detail by Michelsen [26]. However, it is believed that these processes are unimportant under the conditions of low to moderately high laser fluences, a regime the present study concerns. On the left-hand side of Eq. (1), d_{p} is the primary soot particle diameter (typically between 15 and 50 nm for flame

generated soot), ρ_s and c_s are soot particle density and specific heat, and T and t are soot particle temperature and time, respectively. In the laser energy absorption term, $C_a = \pi^2 d_p^3 E(m)/\lambda$ is the absorption cross section of a primary soot particle in the Rayleigh limit which is proportional to the wavelength-dependent soot absorption function $E(m)$ and inversely proportional to the laser wavelength. In this study, the laser wavelength λ is 1064 nm. F_0 is the laser fluence in mJ/mm^2. Function $q(t)$ represents the pulsed laser temporal power density in W/mm^2 per unit laser fluence (mJ/mm^2). Although thermal radiation (incandescence) from the laser heated soot particles is the signal for LII measurements, its contribution to the particle cooling after the laser pulse is negligibly small compared to heat conduction and sublimation at atmospheric pressure. Nevertheless, the radiation heat loss term is included in the present model and calculated according to the expression given in [31]. Under the conditions of an atmospheric pressure laminar diffusion flame investigated in the present study, heat conduction occurs in the free-molecular regime (Knudsen number $Kn \gg 1$). Therefore, the rate of heat conduction can be written as [36]

$$\dot{q}_c = \alpha\pi\left(\frac{d_p}{2}\right)^2 \frac{p_g}{2}\sqrt{\frac{8k_B T_g}{\pi m_g}}\left(\frac{\gamma^*+1}{\gamma^*-1}\right)\left(\frac{T}{T_g}-1\right) \tag{2}$$

where α, p_g and T_g are respectively the thermal accommodation coefficient of soot, the ambient gas pressure, and the gas temperature, k_B the Boltzmann constant, m_g the mass of the surrounding gas molecule, and γ^* average value of the adiabatic constant of the surrounding gas defined as

$$\frac{1}{\gamma^*-1} = \frac{1}{T-T_g}\int_{T_g}^{T}\frac{dT}{\gamma-1} \tag{3}$$

In more general applications of LII for soot or carbon black diagnostics, heat conduction occurs in the transition regime (Knudsen number $Kn \approx 1$) and the Fuch's approach described in [36] should be followed. In the last term of Eq. (1), ΔH_v is the heat of sublimation, i.e. the energy required to sublimate a unit mole of solid carbon into multiple gaseous carbon species, M_v is the average molecular weight of the sublimated gaseous carbon species. The rate of the soot particle mass reduction dM/dt is related to the mass balance of the soot particle written as

$$\frac{dM}{dt} = \frac{1}{2}\rho_s \pi d_p^2 \frac{dd_p}{dt} = -\pi d_p^2 N_v \frac{M_v}{N_A} \tag{4}$$

where N_v is the molecular flux associated with soot sublimation and N_A is Avogadro's constant. Further details of the soot sublimation model can be found in [25].

2.2. Effective particle temperature

When the temperature of soot particles in the laser probe volume is non-uniform, two-color optical pyrometry provides a weighted average or effective particle temperature. In the present study, we consider a uniform spatial laser energy profile and the non-uniformity in soot particle temperature is due to the distribution of the primary soot particle diameter. Once the history of soot particle temperatures is obtained for a range of particle diameters d_p by solving Eqs. (1) and (4), the numerically simulated total LII signals at two different wavelengths in the near-visible spectrum (400 and 780 nm) can be obtained by integrating the thermal emission intensity of soot particles over the entire soot particle ensemble. If we can also assume that soot particles are uniformly distributed inside the laser probe volume and the probe volume is small enough to ensure that the optically thin assumption is valid, the total thermal emission intensity (TEI) at a wavelength λ_i is

$$\mathrm{TEI}_i \propto \int_0^\infty p(d_p)\frac{2\pi c^2 h}{\lambda_i^5}\left[\exp\left(\frac{hc}{\lambda_i k_B T(d_p)}\right)-1\right]^{-1}\frac{\pi^2 d_p^3 E(m_i)}{\lambda_i}dd_p \tag{5}$$

where $p(d_p)$ is the distribution function of the primary soot particle diameter, the soot particle temperature $T(d_p)$ corresponds to the solution of Eqs. (1) and (4) obtained at a laser fluence F_0 (in mJ/mm^2) and primary soot particle diameter d_p. In the present study, a lognormal distribution of primary soot particle diameters is considered following [23,24], and is written as

$$p(d_p) = \frac{1}{d_p\sqrt{2\pi}\ln\sigma_g}\exp\left[-\left(\frac{\ln(d_p/d_g)}{\sqrt{2}\ln\sigma_g}\right)^2\right] \tag{6}$$

where d_g and σ_g are two parameters of the log-normal distribution function and represent respectively the geometric mean particle diameter and the geometric standard deviation. The arithmetic mean primary soot particle diameter d_{10} (the first moment of the distribution function, i.e. $d_{10} = \int_0^\infty d_p p(d_p) dd_p$) and the Sauter mean diameter d_{32} (the ratio of the third to second moments of the distribution function, i.e. $d_{32} = \int_0^\infty p(d_p) d_p^3 dd_p / \int_0^\infty p(d_p) d_p^2 dd_p$) can be related to the two parameters through $d_{10} = d_g \exp[0.5(\ln\sigma_g)^2]$ and $d_{32} = d_g \exp[2.5(\ln\sigma_g)^2]$.

The theoretical effective particle temperature T_e is defined such that it satisfies the following expression

$$\frac{\mathrm{TEI}_1}{\mathrm{TEI}_2} = \frac{E(m_1)}{E(m_2)}\frac{\lambda_2^6}{\lambda_1^6}\frac{\exp(hc/k_B\lambda_2 T_e)-1}{\exp(hc/k_B\lambda_1 T_e)-1} \tag{7}$$

where the subscripts 1 and 2 represent the two detection wavelengths. Eq. (7) is effectively the principle of the two-wavelength optical pyrometer. Substitution of Eq. (5) into Eq. (7) and using the approximation $\exp(hc/\kappa\lambda T) \gg 1$ lead to

$$T_e = C_2\left(\frac{1}{\lambda_2}-\frac{1}{\lambda_1}\right)\Big/\ln\frac{\int_0^\infty p(d_p) d_p^3 \exp\left[-C_2/\lambda_1 T(d_p)\right]dd_p}{\int_0^\infty p(d_p) d_p^3 \exp\left[-C_2/\lambda_2 T(d_p)\right]dd_p} \tag{8}$$

where $C_2 = hc/k_B$. A series of solutions for a range of primary soot particle diameters are first obtained by solving Eqs. (1) and (4). These solutions serve as a database for

the integration in Eq. (8). Unlike the experimentally derived particle effective temperature, the theoretical effective particle temperature is independent of the soot absorption functions at the two detection wavelengths λ_1 and λ_2. However, it is strongly dependent on the soot absorption function at the wavelength of the laser through the laser energy absorption term in Eq. (1). Knowledge of the soot absorption function is one of major sources of uncertainty in both LII model calculations and experiments.

3. Results and discussion

3.1. Solution method

The transient energy equation (1) and the mass equation (4) were solved simultaneously using a first order explicit difference scheme with a variable time step. A very small time step of 0.2 ns was used during and shortly after the laser pulse (up to 50 ns) to resolve the rapid variation of particle temperature. Larger time steps were used after the laser pulse due to slower particle temperature variation. The time steps after the laser pulse were 1 ns (between 50 and 100 ns) and 2 ns (after 100 ns). Temperature-dependent thermal properties including the adiabatic constant, the heat of soot sublimation, the mean molecular weight of the sublimated gaseous species, the vapor pressure, and the specific heat of soot were used. The properties required for the sublimation model were those identified in our previous study [27]. In all the calculations conducted here, the thermal properties of the surrounding gas (the specific heat ratio and the mean mass of gas molecules) were assumed to be the same as those of air. This assumption should not introduce significant error in the numerical results, since these properties of the combustion products at several locations in the atmospheric laminar ethylene–air diffusion flame were found to differ from those of air by only about 2–3% based on local species concentrations from a detailed numerical simulation [37]. The ambient pressure was 1 atm and the local gas temperature was taken to be 1700 K [28]. The density of soot particle was taken to be 1.9 g/cm^3 and the specific heat of soot was taken as that of graphite. The soot absorption function $E(m)$ at 1064 nm (0.4) and the thermal accommodation coefficient of soot particle α (0.37) were taken from our recent study [28]. The spatial profile of the laser is assumed uniform. The temporal profile of the laser power density, corresponding to a laser fluence of 1 mJ/mm^2 (the integration of the curve yields 1 mJ/mm^2), used in the present calculations is shown in Fig. 1. Eq. (1) was solved for 140 primary soot particle diameters in the range of 1–90 nm with non-uniform intervals. These solutions were then used in the numerical evaluation of the integrations in Eq. (8) using a simple trapezoidal algorithm. Unless otherwise indicated, the soot sublimation heat loss term was accounted for in the calculations.

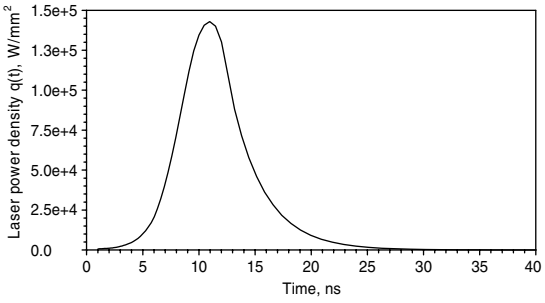

Fig. 1. Temporal profile of the laser power at a laser fluence of 1 mJ/mm^2.

3.2. Critical laser fluence and critical soot particle temperature

The critical laser fluence is defined as the fluence beyond which the soot sublimation becomes important. Knowledge of this critical laser fluence is useful in conducting low-fluence LII experiments. However, it is also important to realize that the critical laser fluence is dependent on the laser temporal profile [25]. The corresponding soot particle temperature is of more general interest since it is an indication if sublimation can be neglected or not, regardless of the properties of the laser used. In order to assess the effect of soot sublimation on the predicted soot particle temperature, numerical calculations were carried out with and without the soot sublimation term for a soot particle diameter of 40 nm and several laser fluences F_0. Some of the results are compared in Fig. 2. These results clearly show that soot sublimation starts to affect the calculated soot particle temperature when the laser fluence F_0 is greater than about 0.95 mJ/mm^2 for the temporal profile of the pulsed laser shown in Fig. 1. The corresponding peak soot particle temperature is about 3300 K, which is regarded as the critical soot particle temperature below which soot sublimation can be neglected, i.e. in the low-fluence LII regime. This critical soot particle temperature is in excellent agreement with that mentioned by Melton [10]. In practical implementation of low-fluence LII where a compromise between achieving a higher signal intensity and reducing the effect of soot sublimation is sought, use of a slightly higher flu-

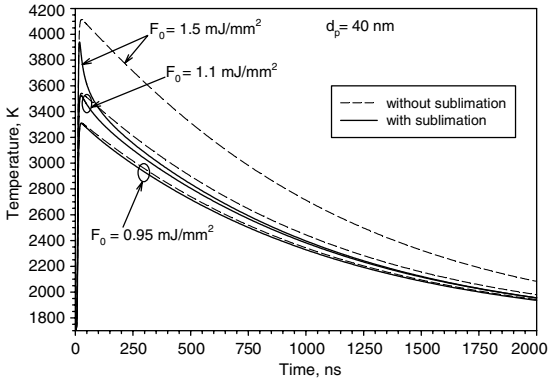

Fig. 2. Histories of a single soot particle temperature calculated at different laser fluences with and without soot sublimation.

ence than 0.95 mJ/mm^2 can still be regarded as in the non-sublimation regime. For example, use of a laser fluence of 1.0 mJ/mm^2, which yields a peak soot particle temperature of about 3400 K, gives rise to a maximum relative error of temperature (between the calculated temperatures with and without soot sublimation term) less than 1.5%. For the slight soot sublimation case of $F_0 = 1.1$ mJ/mm^2, sublimation heat loss enhanced the initial cooling rate of the soot particle but has almost no effect on the peak temperature. For the moderate soot sublimation case of $F_0 = 1.5$ mJ/mm^2, sublimation not only dramatically lowers the soot particle temperature after the peak temperature but also results in a significantly lower peak soot particle temperature.

3.3. Temperature histories of different primary soot particle diameters

The calculated temperature histories of different primary soot particle diameters in the non-sublimation and sublimation regimes are respectively shown in Figs. 3 and 4. It can be seen from both figures that the initial temperature rise curve is identical for different d_p until near the peak values when the laser pulse is nearly over and the cooling processes (surface area-to-volume ratio dependent) start to affect the particle temperature. The temperature of larger particles decays slower than small ones due to smaller surface area-to-volume ratios. The peak temperature increases with the particle diameter and occurs at a slightly longer time after the onset of the laser, especially in the sublimation regime, Fig. 4(b). In the non-sublimation regime, $\ln(T - T_g)$ decays almost linearly with time, Fig. 3(b), i.e. the soot particle temperature T decays almost exponentially. In this regime, it is reasonable to assume that the peak soot particle temperature is independent of the primary soot particle diameter for d_p greater than about 20 nm, see the inset in Fig. 3(a), since the difference in the peak particle temperatures is too small to be practically distinguished. However, this assumption becomes invalid in the sublimation regime, Fig. 4(b), since the peak soot particle temperature increases considerably with increasing d_p.

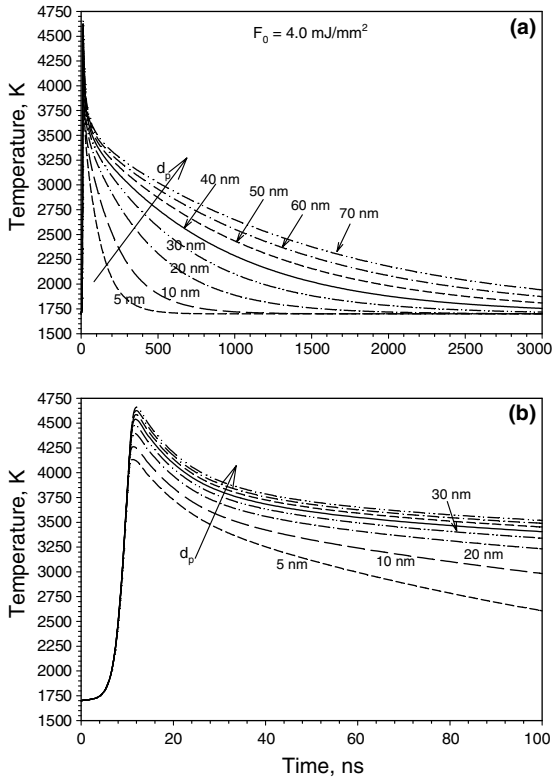

Fig. 4. Temperature histories of different primary soot particle diameters in the sublimation regime.

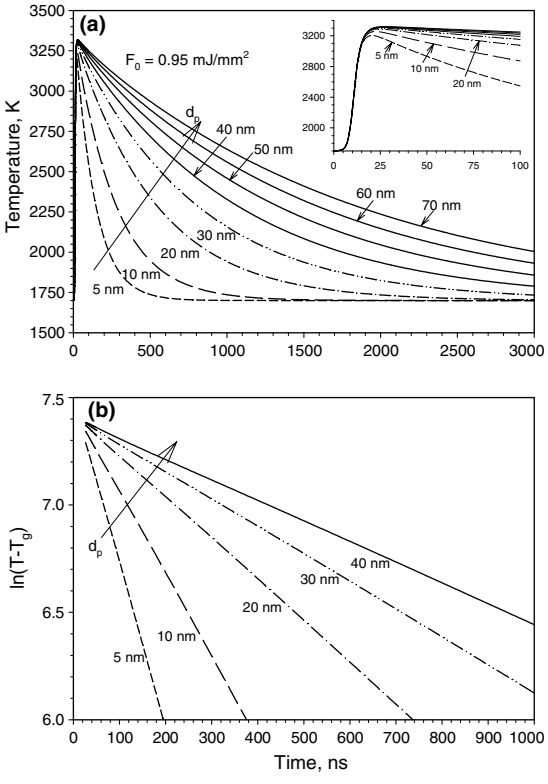

Fig. 3. Temperature histories of different primary soot particle diameters in the non-sublimation regime.

3.4. Effective temperature of different distributions of d_p

In this section, we investigate the effect of the primary soot particle diameter distribution on the calculated history of the effective soot particle temperature determined from the two-color LII signals at 400 nm and 780 nm in the non-sublimation regime, since sublimation not only reduces the primary soot particle diameter but also alters the distribution of d_p due to larger primary particles heating to higher temperatures and losing more mass than smaller particles. The effect of d_p distribution on the effective temperature in the sublimation regime will be studied in the future.

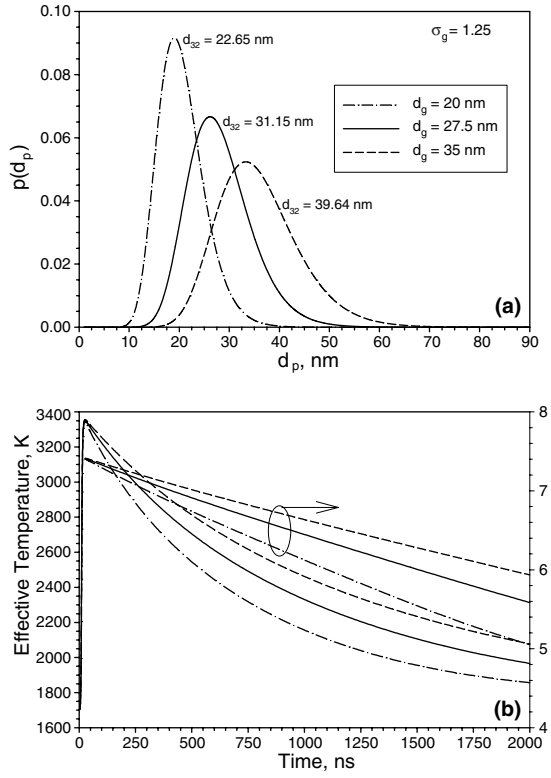

Fig. 5. The distribution function and the effective temperature of soot particle ensembles for different values of d_g: $F_0 = 1$ mJ/mm^2, $\sigma_g = 1.25$.

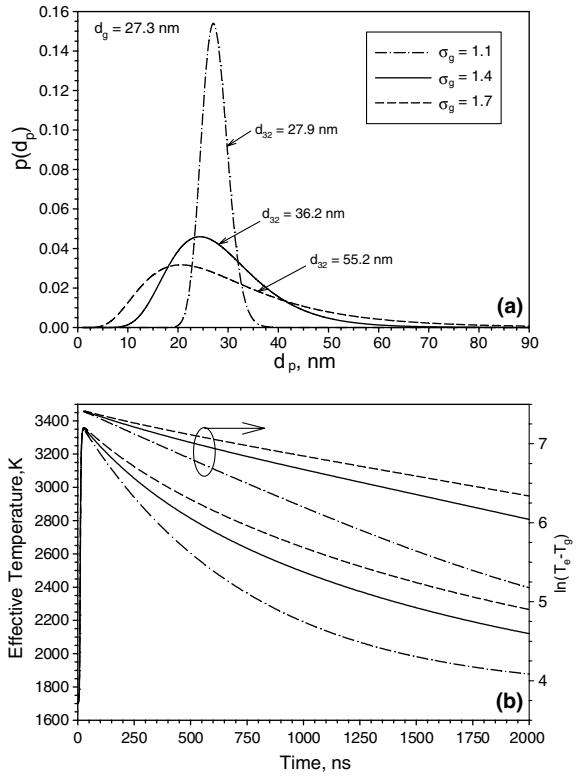

Fig. 6. The distribution function and the effective temperature of soot particle ensembles for different values of σ_g: $F_0 = 1$ mJ/mm^2, $d_g = 27.3$ nm.

Fig. 5 displays the numerical results of the effective soot particle temperature of lognormal distributed soot particles with fixed σ_g and three different d_g. As d_g increases, the distribution function shifts towards larger particles, Fig. 5(a). Since larger particles cool down more slowly, the effective temperature of soot particle ensembles of larger d_g decays slower, Fig. 5(b). Also shown in Fig. 5(b) are the temporal variation of $\ln(T_e - T_g)$. Unlike the almost linear decay of $\ln(T - T_g)$ of monodispersed primary soot particles shown in Fig. 3(a), $\ln(T_e - T_g)$ of polydispersed primary soot particles decays nonlinearly with time with the decay rate gradually decreases. The nonlinear decay of $\ln(T_e - T_g)$ implies that the effective temperature T_e of polydispersed primary soot particles does not decay exponentially with time. In addition, the degree of departure from linearity increases with increasing d_g (for a fixed σ_g). It is also evident from Fig. 5 that the time-resolved temperature of a soot particle ensemble determined by the two-color LII signals can be related to the primary soot particle diameter distribution.

The effect of varying σ_g with a fixed d_g on the effective temperature is shown in Fig. 6. For a fixed d_g, an increase in σ_g results in increased mean particle diameters (both d_{10} and d_{32}). This is associated with the enhanced wing of the distribution at large diameters as σ_g increases, Fig. 6(a). The biased contribution from the wing of the lognormal distribution (corresponding to larger and hotter particles) to the effective temperature causes the decay rate of T_e to be slower for larger σ_g, Fig. 6(b). For the narrowest distribution considered, i.e. $\sigma_g = 1.1$, $\ln(T_e - T_g)$ decays almost linearly with time, implying that the polydispersity of this distribution can be neglected. For the other two distributions considered, however, $\ln(T_e - T_g)$ exhibits stronger non-linearity.

The distribution functions of d_p and the corresponding effective temperature of soot particle ensembles for fixed d_{10} are displayed in Fig. 7. The Sauter mean diameter of each distribution, d_{32}, is also indicated in the figure, Fig. 7(a). In the narrowest distribution of d_p considered (the solid line), the primary soot particle can be approximately treated as monodispersed. These results imply that the two-color LII inferred soot particle temperature decay curve alone cannot be used to estimate the mean primary soot particle diameter unless the distribution of primary soot particle diameter is sufficiently narrow. For soot generated in an atmospheric pressure laminar and turbulent diffusion flames in a given location, the primary particle diameters were found to have a relatively narrow distribution with standard deviations of about 20% of the mean diameter (d_{10}) based on thermophoretic sampling/transmission electron microscopy analysis [38,39]. These experimental findings correspond approximately to the case of $\sigma_g = 1.25$ shown in Fig. 7 (dashed line). In other words, the effect of the primary soot particle diameter distribution on the two-color LII derived effective temperature cannot be neglected, since the dashed-line curve in Fig. 7(b) departs significantly from the solid-line curve. If the

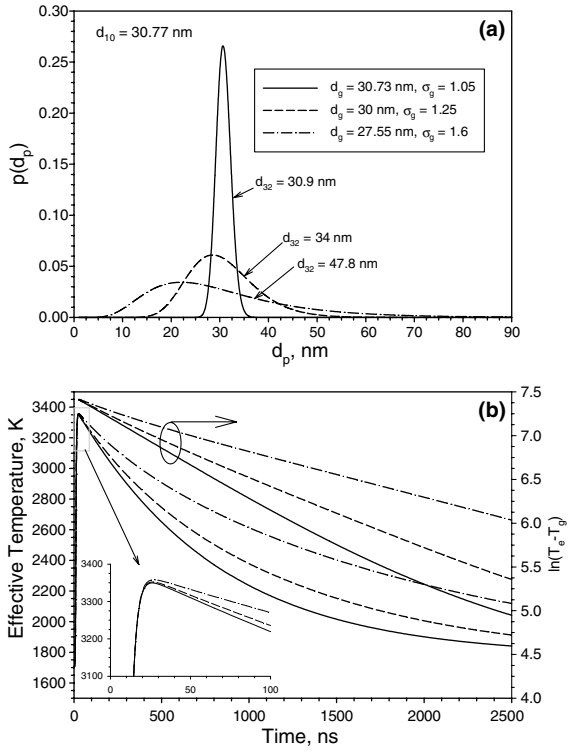

Fig. 7. The distribution functions and the corresponding effective temperature of soot particle ensembles for a fixed d_{10}: $F_0 = 1$ mJ/mm^2, $d_{10} = 30.77$ nm.

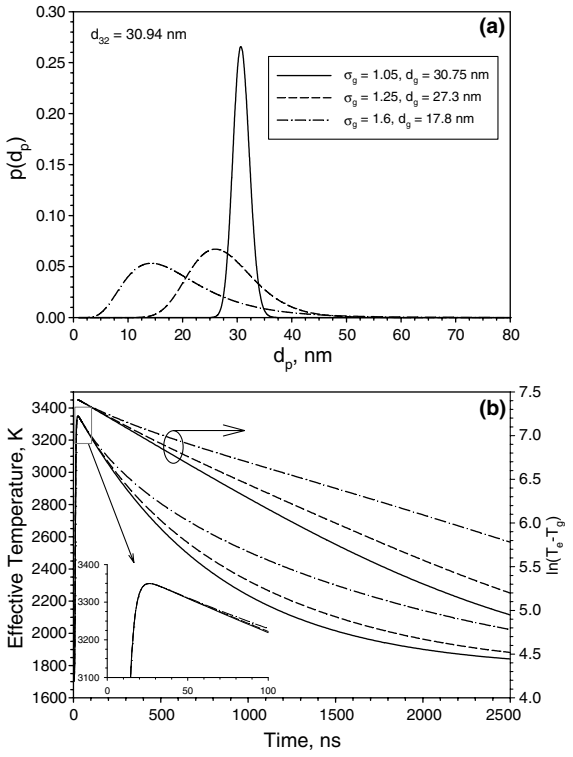

Fig. 8. The distribution functions and the corresponding effective temperature of soot particle ensembles for a fixed d_{32}: $F_0 = 1$ mJ/mm^2, $d_{32} = 30.94$ nm.

dashed-line effective temperature decay curve shown in Fig. 7(b) were used as the experimental data to estimate the mean primary soot particle diameter, an inaccurate (somewhat larger) particle diameter would be recovered. Fig. 7(b) also shows that the initial temperature decay rate right after the moment of the peak temperature (see the inset) is quite different even for these three soot particle ensembles which have the same mean diameter d_{10}. A comparison between the initial temperature decay rates and the Sauter mean diameters (d_{32}) of these three distributions reveals that the effective temperature of a soot particle ensemble with a larger d_{32} decays slower than that with a smaller d_{32}. This is also true for the results shown in Figs. 5 and 6. Except for the narrowest distribution, the solid line shown in Fig. 7(a) and (b), whose $\ln(T_e - T_g)$ decays nearly linearly with time, $\ln(T_e - T_g)$ of the two wider distributions varies nonlinearly with time.

To further explore the relationship between the initial effective temperature decay rate and the Sauter mean diameter of a soot particle ensemble, numerical calculations were conducted for three different distributions of primary soot particle diameter with a fixed Sauter mean diameter of $d_{32} = 30.94$ nm and the results are shown in Fig. 8. It is interesting to note that the initial effective temperature decay rates of these three soot particle ensembles are essentially identical. This is a very useful finding in applying the two-color LII derived effective temperature curve for soot particle sizing. The numerical results shown in Fig. 8 suggest that the experimentally determined initial temperature decay rate can be used unambiguously to obtain the Sauter mean diameter of the soot particle ensemble. At longer times, the effective temperatures or $\ln(T_e - T_g)$ of different d_p distributions start to exhibit increasingly large difference with time.

To understand why the initial temperature decay rate is related to the Sauter mean diameter of the soot particle ensemble and establish the quantitative relationship between the initial effective temperature decay rate and the Sauter mean diameter, a theoretical analysis of the two-color LII effective temperature was conducted. Differentiation of the effective temperature given in Eq. (8) with respect to time leads to

$$\frac{dT_e}{dt} = \frac{C_2\left(\frac{1}{\lambda_1} - \frac{1}{\lambda_2}\right)}{\left(\ln\frac{\int_0^\infty p(d_p)d_p^3 e^{-C_2/\lambda_1 T(d_p)} dd_p}{\int_0^\infty p(d_p)d_p^3 e^{-C_2/\lambda_2 T(d_p)} dd_p}\right)^2} \times \left[\frac{\int_0^\infty e^{-C_2/\lambda_1 T(d_p)}\left(\frac{C_2}{\lambda_1}\frac{1}{T^2}\frac{dT}{dt}\right)p(d_p)d_p^3 dd_p}{\int_0^\infty e^{-C_2/\lambda_1 T(d_p)}p(d_p)d_p^3 dd_p} - \frac{\int_0^\infty e^{-C_2/\lambda_2 T(d_p)}\left(\frac{C_2}{\lambda_2}\frac{1}{T^2}\frac{dT}{dt}\right)p(d_p)d_p^3 dd_p}{\int_0^\infty e^{-C_2/\lambda_2 T(d_p)}p(d_p)d_p^3 dd_p}\right] \quad (9)$$

In the non-sublimation regime and at the moment of the peak soot particle temperature τ_{max}, the energy balance equation, Eq. (1), can be re-written as

$$\frac{1}{6}\pi d_p^3 \rho_s c_s \left.\frac{dT}{dt}\right|_{\tau_{max}} = -\alpha\pi\left(\frac{d_p}{2}\right)^2 \frac{p_g}{2}\sqrt{\frac{8k_B T_g}{\pi m_g}}\left(\frac{\gamma^*+1}{\gamma^*-1}\right)\left(\frac{T_{max}}{T_g}-1\right) \quad (10)$$

where T_{max} represents the peak soot particle temperature and can be treated as independent of the primary soot particle diameter as shown in Fig. 3. Eq. (10) defines the initial temperature decay rate for monodispersed primary soot particle of diameter d_p, i.e.

$$\left.\frac{dT}{dt}\right|_{\tau_{max}} = -\frac{\Theta(T_{max}-T_g)}{d_p} \quad (11)$$

where Θ is defined as

$$\Theta = \frac{3\alpha p_g}{4\rho_s c_s T_g}\sqrt{\frac{8k_B T_g}{\pi m_g}}\left(\frac{\gamma^*+1}{\gamma^*-1}\right) \quad (12)$$

The initial effective temperature decay rate at the moment of the peak soot particle temperature τ_{max} can now be obtained by substituting Eq. (11) into Eq. (9) and making use of the assumption that at τ_{max} all the soot particles of different d_p have the same temperature T_{max} and the definition of d_{32}

$$\left.\frac{dT_e}{dt}\right|_{\tau_{max}} = -\frac{\Theta(T_{max}-T_g)}{d_{32}} \quad (13)$$

Eq. (13) can also be conveniently written in terms of $\ln(T_e - T_g)$ as

$$\left.\frac{d\ln(T_e-T_g)}{dt}\right|_{\tau_{max}} = -\frac{\Theta}{d_{32}} \quad (14)$$

Eq. (13) or Eq. (14) indicates that the initial decay rate of a soot particle ensemble at the moment of the peak soot particle temperature is inversely proportional to the Sauter mean diameter of the polydispersed primary soot particles. With consideration of the theoretical initial effective temperature decay rate given in Eq. (13), the numerical results shown on Figs. 5–8 can be better understood in view of the importance of d_{32} to the overall history of the effective temperature.

3.5. Variation of the peak soot particle temperature with laser fluence

Variation of the peak effective temperature with the laser fluence F_0 is shown in Fig. 9. Numerical calculations were conducted for laser fluences between 0.5 and 1.0 mJ/mm^2. The upper limit is defined by the critical peak soot particle temperature (about 3300 K) below which soot sublimation can be neglected. The lower limit is set somewhat arbitrarily but primarily based on the considerations that accurate LII signals are difficult to acquire experimentally at soot particle temperatures below about 2500 K due to deteriorating signal-to-noise ratio. These results were obtained for lognormal distributed primary soot particles with $d_g = 30$ nm and $\sigma_g = 1.25$, typical of flame generated soot particles (see the dashed-line curve in Fig. 7(a)). It was shown in our previous study [28] that the peak soot particle temperature in the non-sublimation regime can be approximately written as

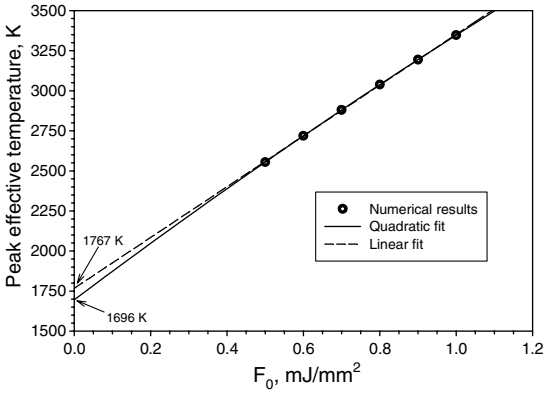

Fig. 9. Variation of the peak soot particle temperature in the non-sublimation regime with the laser fluence F_0: $d_g = 30$ nm, $\sigma_g = 1.25$.

$$T_{max} = T_g + \frac{6\pi E(m)F_0}{\lambda\rho_s c_s}\int_0^{\tau_{max}} q(t)\,dt \quad (15)$$

An examination of the numerical results indicates that the peak effective temperature occurs at a time of $\tau_{max} =$ 26.4 ns for laser fluences between 0.5 and 1.0 mJ/mm^2, which is effectively at the end of the laser pulse displayed in Fig. 1. Eq. (15) implies that the peak temperature should vary linearly with the laser fluence F_0 if the properties of soot (ρ_s and c_s) are independent of temperature. However, as a result of employing a temperature-dependent specific heat of soot (while the density of soot is assumed constant), it was found that a quadratic variation of T_{max} with F_0 yields a better fit to the numerical results than the linear assumption. Extrapolation of the quadratic fit or the linear fit to the numerical results to $F_0 = 0$ should yield the local gas temperature T_g. The quadratic fit yields a local gas temperature of 1696 K, which is in excellent agreement with the input gas temperature of 1700 K, while the linear fit yields a somewhat higher gas temperature of 1767 K. The reproduction of the local gas temperature from the extrapolation of the quadratic fit is also an indication that the quadratic fit to the peak soot particle temperatures should in general be assumed. Results shown in Fig. 9 outline the principle of measuring the local gas temperature using low-fluence LII under steady-state conditions. Experimentally the peak soot particle temperatures at a series of laser fluences in the non-sublimation regime are first obtained. These experimental data points are then fit to a quadratic function. Extrapolation of the quadratic fit to zero laser fluence yields the local gas temperature.

3.6. A simple approach to apply low-fluence LII for primary soot particle sizing

Based on the numerical and theoretical results presented above, a simple approach is proposed to infer the primary

soot particle diameter distribution based on the time-resolved two-color LII determined effective temperature of a soot particle ensemble. We assume the distribution of the primary soot particles follows the lognormal function. The approach is based on the following two important observations from results shown in Figs. 7 and 8: (i) the initial decay rate right after the peak effective temperature is related to the Sauter mean diameter of the soot particle ensemble, but not the arithmetic mean diameter, as confirmed from the theoretical analysis given in Eq. (13), and (ii) the effective temperature of a soot particle ensemble exhibits a maximum sensitivity to the distribution of d_p at some time τ_c after the peak temperature. Under the conditions of the atmospheric pressure laminar diffusion flame considered here, the effective temperatures of different distributions of d_p show the largest difference around $\tau_c = 1.5\mu s$, Fig. 8. This approach requires the knowledge of the local gas temperature T_g, the thermal accommodation coefficient of soot α, the experimentally measured peak soot particle temperature T_{max}, and the initial temperature decay rate dT_e/dt, as well as the effective temperature at time τ_c. The present approach to use the two-color LII derived effective temperature as a primary soot particle sizing tool can be summarized as follows. First, determine the Sauter mean diameter d_{32} from Eq. (13) or Eq. (14) using the experimental data of T_{max} and dT_e/dt. With an initial estimate of σ_g^* likely for soot, for example $\sigma_g^* = 1.2$, calculate d_g from $d_{32} = d_g \exp[2.5(\ln \sigma_g)^2]$. For this fixed d_g, calculate the theoretical effective temperatures at τ_c (here about 1.5 μs) at a series of σ_g, similar to Fig. 6. By matching the theoretical effective temperature at τ_c to the experimental value, a new σ_g can be determined. This procedure repeats until a converged value of σ_g is obtained.

The primary soot particle sizing approach described above was applied to obtain the soot particle diameter distribution at 42 mm above the burner exit surface and along the flame axis in an atmospheric pressure ethylene/air diffusion flame investigated previously [28]. At this flame location, ex situ measurement of the primary soot particle diameter distribution has been carried out using thermophoretic sampling/transmission electron microscopy analysis [39]. The peak two-color LII experimentally determined soot particle temperature at this location is about 3015 K and the temperature at 1.515 μs is about 2104 K, see Fig. 10. The almost top-hat laser spatial intensity profile used in the experiment [28] was simulated by uniform laser fluence. An effective laser fluence of 0.765 mJ/mm^2 was required in the calculation to reproduce the experimentally observed peak soot particle temperature. The corresponding initial temperature decay rate (for data up to 100 ns) and the coefficient in Eq. (13) were found to be $dT_e/dt = -1.28$ K/ns and $\Theta = 0.036332$ m/s, respectively. The LII inferred Sauter mean diameter is therefore $d_{32} = 37.33$ nm. With an initial estimate of $\sigma_g^* = 1.2$, about 6–7 iterations were found to be sufficient to achieve converged lognormal parameters of $d_g = 31.43$ nm and $\sigma_g = 1.30$, which reproduce the experimental effective temperature of 2104 K at 1.515 μs and the Sauter mean diameter (37.33 nm) of the primary soot particle diameter distribution. The predicted effective soot particle temperature at this location in the flame is compared with the experimental data [28] in Fig. 10. Overall excellent agreement is observed between the numerical results and the experimental data. To quantitatively assess the quality of this primary soot particle diameter distribution, the error between the experimental particle temperature and the numerically calculated one, defined below, was evaluated for distribution parameters in the vicinity of $d_g = 31.43$ nm and $\sigma_g = 1.30$

$$\varepsilon = \sum_{i=1}^{N} \left[T_{e,\exp} - T_e(\sigma_g, d_g)\right]^2 \tag{16}$$

where N (680 in this study) is the number of experimental points between 26.4 ns and 3000 ns. The results are shown in Fig. 11. It can be seen that the log-normal distribution parameters obtained above, i.e. $d_g = 31.43$ nm and $\sigma_g = 1.30$, are clearly not the optimal parameters in terms of the minimization of the error defined above, but the error associated with these parameters is only slightly larger than

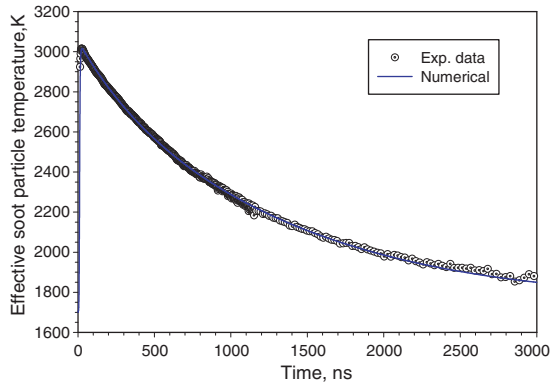

Fig. 10. Comparison of the predicted effective soot particle temperature with the experimental data in the atmospheric pressure laminar diffusion flame.

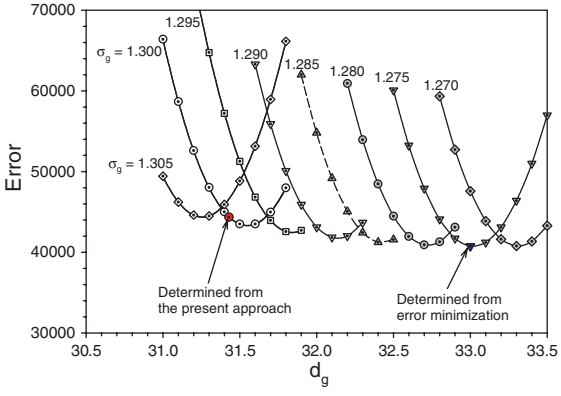

Fig. 11. Variation of error with parameter $d\sigma_g$ for three different σ_g in the neighborhood of $d_g = 31.43$ nm and $\sigma_g = 1.30$. The minimum error occurs at $d_g = 33.0$ nm and $\sigma_g = 1.275$.

the minimum error at the optimized log-normal distribution parameters of $d_g = 33.0$ nm and $\sigma_g = 1.275$. However, the Sauter mean diameter of this optimized log-normal distribution (38.25 nm) is slightly larger than that determined from the initial experimental particle temperature decay rate (37.33 nm). Due to various experimental uncertainties, it is very likely that the log-normal d_p distribution determined from the present soot particle sizing approach, which ensures that the calculated initial temperature decay rate is the same as the experimental one, is not identical to that determined from the two-variable optimization. Nevertheless, given such small differences between the log-normal distribution parameters determined from the present approach and those from the two-variable optimization, it can be concluded that the present approach is consistent with the multi-variable optimization technique used recently by Lehre et al. [22,23]. However, the present approach is simpler and computationally more efficient. In addition, the present approach has advantages for practical measurements where the signal quality is poor at low temperatures/long times and the low temperature data could significantly affect the results from the multivariable optimization technique.

The inferred primary soot particle diameter distributions from the experimental time-resolved soot particle temperature using the present approach is compared with the ex situ measurement reported in [39] in Fig. 12. It is evident that the d_p distribution obtained by the present approach is very similar to and slightly better than that reached by the error minimization, judged by the location of the peak of the distribution. When plotted in Fig. 10, the effective temperature history of the optimized d_p distribution, i.e. $d_g = 33.0$ nm and $\sigma_g = 1.275$, was found to be almost identical to that determined using the present approach. Although the overall agreement is seen to be reasonable, the distribution of d_p from the present approach has a significantly greater population of larger particles (diameter greater than about 35 nm) than the ex situ measurements. This is actually expected since the shielding effect, which reduces the rate of conduction heat loss of soot aggregates to the surrounding gas, is not taken into account. As a result, a higher population of larger particles is required to compensate for the neglect of the shielding effect. The shielding effect due to aggregated soot particles is currently being incorporated into the present laser-induced incandescence model.

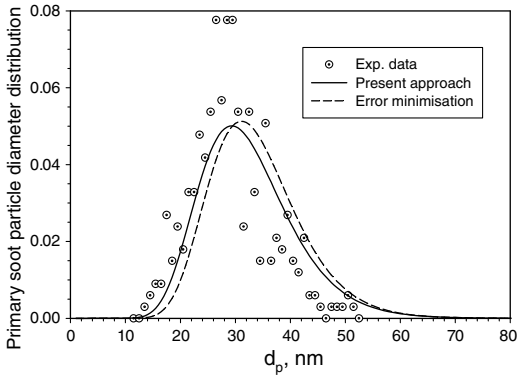

Fig. 12. Comparison of the LII derived primary soot particle diameter distributions with the experimental data based on thermophoretic sampling/transmission electron microscopy analysis.

4. Conclusions

Detailed numerical calculations were conducted in this study using a single particle based laser-induced incandescence model and the best available optical and thermal properties of soot. The critical soot particle temperatures were found to be about 3300–3400 K, above this temperature range soot sublimation has to be accounted for to accurately predict the particle temperature history. In the non-sublimation regime, the peak soot particle temperature can be assumed to be independent of the primary particle diameter. This assumption becomes less valid in the sublimation regime. In the non-sublimation regime, the initial decay rate right after the peak temperature of polydispersed soot particles is inversely proportional to the Sauter mean diameter, rather than the arithmetic mean diameter. For different primary soot particle distributions of similar Sauter mean diameters, although there is little difference in the effective soot particle temperatures in the early stages of temperature decay, this difference becomes significantly larger later in the decay, and eventually the difference begins to diminish at long decay times. A simple primary soot particle sizing technique was proposed based on these two observations. Application of this approach to an atmospheric pressure laminar diffusion flame yields a primary soot particle diameter distribution in reasonable agreement with ex situ experimental measurement. The present particle sizing technique is consistent with but simpler and more computationally efficient than the multi-variable optimization technique. The primary particle sizing technique proposed in this study can also be applied to other nanoparticles in conjunction with time-resolved two-wavelength laser-induced incandescence measurement.

References

[1] R.J. Santoro, H.G. Semerjian, R.A. Dobbins, Soot particle measurements in diffusion flames, Combust. Flame 51 (1983) 203–218.
[2] Ü.Ö. Köylü, G.M. Faeth, Optical properties of soot in buoyant laminar diffusion flames, J. Heat Transfer 116 (1994) 971–979.
[3] R.A. Dobbins, C.M. Megaridis, Morphology of flame-generated soot as determined by thermophoretic sampling, Langmuir 3 (1987) 254–259.
[4] B. Quay, T.-W. Lee, T. Ni, R.J. Santoro, Spatially resolved measurements of soot volume fraction using laser-induced incandescence, Combust. Flame 97 (1994) 384–392.
[5] R.L. Vander Wal, K.J. Weiland, Laser-induced incandescence: development and characterization towards a measurement of soot-volume fraction, Appl. Phys. B 59 (1994) 445–452.
[6] C.R. Shaddix, K.C. Smyth, Laser-induced incandescence measurements of soot production in steady and flickering methane, propane,

and ethylene diffusion flames, Combust. Flame 107 (1996) 418–452.
[7] D.R. Snelling, G.J. Smallwood, I.G. Campbell, J.E. Medlock, Ö.L. Gülder, in: AGARD 90th Symposium of the Propulsion and Energetics Panel on Advanced Non-intrusive Instrumentation for Propulsion Engines, Brussels, Belgium, 1997.
[8] D.R. Snelling, G.J. Smallwood, R.A. Sawchuk, W.S. Neill, D. Gareau, D. Clavel, W.L. Chippior, F. Liu, Ö.L. Gülder, W.D. Bachalo, In-situ real-time characterization of particulate emissions from a diesel engine exhaust by laser-induced incandescence, SAE Paper 2000-01-1994, 2000.
[9] R.W. Weeks, W.W. Duley, Aerosol-particle sizes from light emission during excitation by TEA CO_2 laser pulses, J. Appl. Phys. 45 (10) (1974) 4661–4662.
[10] L.A. Melton, Soot diagnostics based on laser heating, Appl. Opt. 23 (13) (1984) 2201–2208.
[11] S. Will, S. Schraml, A. Leipertz, Two-dimensional soot-particle sizing by time-resolved laser-induced incandescence, Opt. Lett. 20 (22) (1995) 2342–2344.
[12] N.P. Tait, D.A. Greenhalgh, PLIF imaging of fuel fraction in practical devices and LII imaging of soot, Ber. Bunsenges. Phys. Chem. 97 (12) (1993) 1619–1625.
[13] P. Roth, A.V. Filippov, In situ ultrafine particle sizing by a combination of pulsed laser heatup and particle thermal emission, J. Aerosol Sci. 27 (1) (1996) 95–104.
[14] S. Will, S. Schraml, A. Leipertz, Comprehensive two-dimensional soot diagnostics based on laser-induced incandescence (LII), Proc. Combust. Inst. 26 (1996) 2277–2284.
[15] B. Mewes, J.M. Seitzman, Soot volume fraction and particle size measurements with laser-induced incandescence, Appl. Opt. 36 (3) (1997) 709–717.
[16] R.L. Vander Wal, T.M. Ticich, A.B. Stephens, Can soot primary particle size be determined using laser-induced incandescence? Combust. Flame 116 (1999) 291–296.
[17] A.V. Filippov, M.W. Markus, P. Roth, In-situ characterization of ultrafine particles by laser-induced incandescence: sizing and particle structure determination, J. Aerosol Sci. 30 (1) (1999) 71–87.
[18] D. Woiki, A. Giesen, P. Roth, Time-resolved laser-induced incandescence for soot particle sizing during acetylene pyrolysis behind shock waves, Proc. Combust. Inst. 28 (2000) 2531–2537.
[19] B. Axelsson, P.E. Bengtsson, Laser-induced incandescence for soot particle size and volume fraction measurements using on-line extinction calibration, Appl. Phys. B (Lasers and Optics) 72 (2001) 361–372.
[20] S. Dankers, S. Schraml, S. Will, A. Leipertz, Application of laser-induced incandescence for the determination of primary particle sizes of nanoparticles demonstrated using carbon blacks, Chem. Eng. Technol. 25 (2002) 1160–1164.
[21] A. Leipertz, S. Dankers, Characterization of nano-particles using laser-induced incandescence, Part. Part. Syst. Charact. 20 (2003) 81–93.
[22] T. Lehre, H. Bockhorn, B. Jungfleisch, R. Suntz, Development of a measuring technique for simultaneous in situ detection of nanoscaled particle size distributions and gas temperatures, Chemosphere 51 (2003) 1055–1061.
[23] T. Lehre, B. Jungfleisch, R. Suntz, H. Bockhorn, Size distributions of nanoscaled particles and gas temperatures from time-resolved laser-induced-incandescence measurements, Appl. Opt. 42 (12) (2003) 2021–2030.
[24] S. Dankers, A. Leipertz, Determination of primary particle size distributions from time-resolved laser-induced incandescence measurements, Appl. Opt. 43 (18) (2004) 3726–3731.
[25] D.R. Snelling, F. Liu, G.J. Smallwood, Ö. L. Gülder, Evaluation of the nanoscale heat and mass transfer model of LII: prediction of the excitation intensity, NHTC2000-12132, in: Proceedings of NHTC'00, 34th National Heat Transfer Conference, Pittsburgh, PA, 2000.
[26] H.A. Michelsen, Understanding and predicting the temporal response of laser-induced incandescence from carbonaceous particles, J. Chem. Phys. 118 (15) (2003) 7012–7045.
[27] G.J. Smallwood, D.R. Snelling, F. Liu, Ö.L. Gülder, Clouds over soot evaporation: errors in modeling laser-induced incandescence of soot, J. Heat Transfer 123 (4) (2001) 814–818.
[28] D.R. Snelling, F. Liu, G.J. Smallwood, Ö.L. Gülder, Determination of the soot absorption function and thermal accommodation coefficient using low-fluence LII in a laminar coflow ethylene diffusion flame, Combust. Flame 136 (2004) 180–190.
[29] D.R. Snelling, G.J. Smallwood, Ö.L. Gülder, F. Liu, Small particle analysis by laser induced incandescence, US Patent No. 6,809,820 B2, October, 2004.
[30] D.L. Hofeldt, Real-time soot concentration measurement technique for engine exhaust streams, SAE Technical paper Series 930079, 1993, pp. 33–45.
[31] F. Liu, G.J. Smallwood, D.R. Snelling, Effects of primary particle diameter and aggregate size distribution on the temperature of soot particles heated by pulsed lasers, J. Quant. Spectroscopy Radiative Transfer 93 (2005) 301–312.
[32] A.C. Eckbreth, Effects of laser-modulated particulate incandescence on Raman scattering diagnostics, J. Appl. Phys. 48 (11) (1977) 4473–4479.
[33] M.G. Allen, B.L. Upschulte, D.M. Sonnenfroh, W.T. Rawlins, C. Gmachl, F. Capasso, A. Hutchinson, D. Sivco, A. Cho, Infrared characterization of particulate and pollutant emissions from gas turbine combustors, AIAA paper 2001-0789, 2001.
[34] B.F. Kock, C. Kayan, J. Knipping, H.R. Orthner, P. Roth, Comparison of LII and TEM sizing during synthesis of iron particle chains, Proc. Combust. Inst. 30 (2005) 1689–1697.
[35] T. Lehre, R. Suntz, H. Bockhorn, Time-resolved two-color LII: size distributions of nano-particles from gas-to-particle synthesis, Proc. Combust. Inst. 30 (2005) 2585–2593.
[36] A.V. Filippov, D.E. Rosner, Energy transfer between an aerosol particle and gas at high temperature ratios in the Knudsen transition regime, Int. J. Heat Mass Transfer 43 (2000) 127–138.
[37] F. Liu, H. Guo, G.J. Smallwood, Ö.L. Gülder, Effects of gas and soot radiation on soot formation in a coflow laminar ethylene diffusion flame, J. Quant. Spectroscopy Radiative Transfer 73 (2002) 409–421.
[38] Ü.Ö. Köylü, G.M. Faeth, Structure of overfire soot in buoyant turbulent diffusion flames at long residence times, Combust. Flame 89 (1992) 140–156.
[39] K. Tian, F. Liu, K.A. Thomson, D.R. Snelling, G.J. Smallwood, D. Wang, Distribution of the number of primary particles of soot aggregates in a nonpremixed laminar flame, Combust. Flame 138 (2004) 195–198.